Journal of the Korean Nuclear Society
Volume 34, Number 6, pp.574~585, December, 2002

Evaluation of Mechanical Properties of RPV Clad by Small Punch Tests

Joo Suk Lee and In Sup Kim
Korea Advanced Institute of Science and Technology
373-1 Guseung-dong, Yuseung-gu Daejeon, Korea 305-701
jslee@mail.kaist.ac.kr

(Receved July 4, 2002)

Abstract

The microstructural characteristics and its related mechanical properties of RPV cladding have been investigated using small punch (SP) tests. SA508 Cl.3 RPV steel plates were overlay cladded with the type ER309L welding consumables by submerged arc welding process. Although the RPV clad material had a small portion of δ ferrite phase, it still showed the ductile to brittle transition behavior. The transition temperature was determined by the SP test and it depended on the content of σ phase, specimen size, and determination methods. The fracture appearance of SP specimen was changed from circumferential to radial cracking as test temperature became low, and below the transition temperature region, ER309L cladding usually fractured along the δ ferrite by the low temperature failure of ferrite phase.

Key Words : RPV clad, δ ferrite, σ phase, small punch test, SP-DBTT

1. Introduction

The inner wall of reactor pressure vessel (RPV) was overlay cladded with 300 grade austenitic stainless steels of a few millimeter thickness to prevent the general corrosion attack and the radioactive contamination problems in main coolant systems. However, it has been reported that δ ferrite in the RPV clad, which was generated during overlay welding practice, could induce thermal aging and irradiation embrittlement during in-service period [1-4]. Small amount of δ ferrite is desirable in the weld zones of austenitic stainless steels, because the ferrite phase prevents hot tearing or cracking. But, δ ferrite is likely to decompose to brittle σ phase, austenite, and chromium rich carbide if it is exposed to the temperature range between 600 ℃ and 900 ℃ [5, 6]. Although some irradiation and thermal aging embrittlement researches have been done on the RPV clad, it is still insufficient to explain the microstructural characteristics and their related effects on the mechanical properties.

Since 1970's small punch (SP) test has been developed to estimate and correlate to the conventional mechanical properties such as yield and tensile strengths, ductile to brittle transition temperature, and fracture toughness [7-9]. And,

Table 1. The Chemical Composition of AWS Class ER309L Weld Consumable

C	Si	Mn	P	S	Cr	Ni	Mo
0.011	0.36	1.60	0.013	0.001	23.77	13.19	0.06
Co	V	Ti	Cu	Nb	N	Fe	
0.026	0.052	0.09	0.039	<0.01	0.045	bal.	

Table 2. Volumetric Phase Fractions and Tensile Properties of RPV Clad Depending on Maximum Heatlinput Rates

Index	Max. heat input (kJ/cm)	*FN	FN (after PWHT)	σ phase (vol. %)	Yield Strength (MPa)	Tensile strength (MPa)
K001	164.4	9.1	6.6	1.9	301.2	523.9
K002	188.5	10.2	6.0	3.7	319.5	540.3

*FN; ferrite number measured by magnetic gage, which almost equals to the volumetric percent.

Table 3. Heat Treatment Conditions During Overlay Welding and Postweld Heat Treatment

Preheating	121℃ min
Inter-pass heating	176℃ max.
Posting Heating	210~310℃/ 2 hours
Postweld Heat Treatment (PWHT)	620~628℃ / 41 hours

the SP test proved an effective method to determine the degree of thermal aging embrittlement of a duplex stainless steel [10].

The objective of the present paper is to clarify the microstructural characteristics and its related mechanical properties of the RPV cladding using small punch tests. Two kinds of stainless steel weld overlay clad were fabricated by the submerged arc welding (SAW) differing in maximum heat input rate.

2. Experimental

2.1. Material Preparation

The welding consumable metal of American Welding Society (AWS) Class ER309L stainless steel was chosen as applied in nuclear industry. The chemical composition of ER309L is given in Table1. The cladding was deposited with the submerged arc welding (SAW) process on SA508 Cl.3 plates that were 100 mm thick 300 mm wide and 500 mm long to minimize distortion and to provide heat sink. The welding parameters such as current, voltage and welding speed, and two kinds of maximum heat input rates were chosen (Table 2). The clad thickness was about 6 millimeter. Heat treatment conditions during overlay welding and postweld heat treatment (PWHT) are illustrated in Table 3.

Observation of microstructure of clad metals was done using optical and scanning electron microscopes (SEM) after etching in a solution of 15 ml HCl + 5 ml HNO_3.

2.2. SP Test Procedure

Transmission Electron Microscopy (TEM) disk (3 mmϕ × 0.28 mm) and coupon type (10 × 10 × 0.5 mm^3) small punch (SP) specimens were sampled from 2 mm away from the weld fusion line. SP test was performed with an Instron 4204 at a cross-head speed of 0.2 mm/min for TEM disk and 0.4 mm/min for coupon type specimens at temperatures from ~87K to 293K. Temperature was controlled by injection of liquid nitrogen into a nitrogen tank with argon gas environment. Fig. 1 shows the schematic drawing of the SP test cell. Steel balls of different diameters were employed for loading fixtures; 2.4 mm for coupon type, and 1 mm for TEM disk type specimens. Hardness values of these steel balls were over conventional hardness Rockwell (HRC) 60. Displacements were measured using linear variable differential transducer (LVDT) and movement of cross-head. The LVDT is placed under the specimen, touching the bottom surface of the specimen.

Two kinds of specimen holder were used for SP test using an Instron 4204 machine. The holder for TEM disk type specimen consists of a die with a central hole of 1.6 mm in diameter and a clamping screw with a hole of 1mm in diameter for guiding the ball and loading pin. The holder for coupon type specimen consists of a 2.4 mm in diameter punch, upper die, and lower die with a hole 4 mm in diameter. SEM was used to observe the fracture mode and fracture surface of SP specimens.

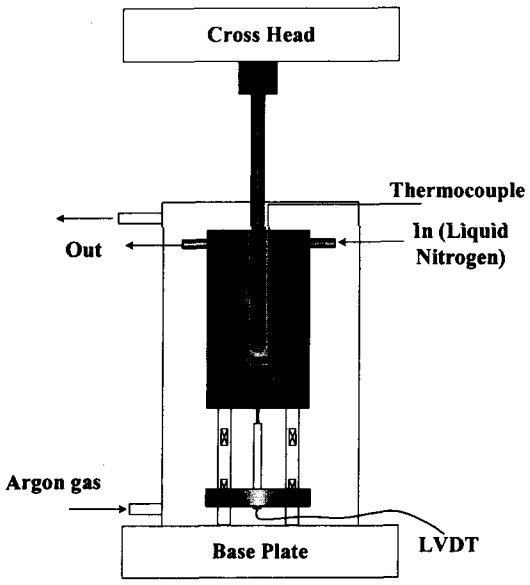

Fig. 1. Schematic Drawing of the Small Punch (SP) Test Cell

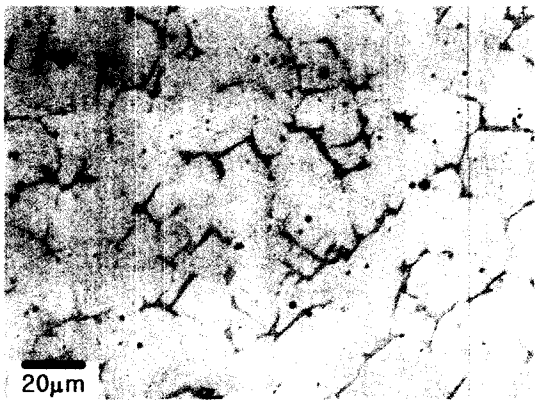

(a)

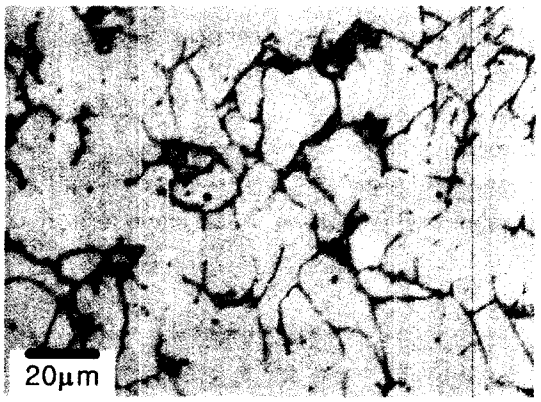

(b)

Fig. 2. Optical Micrographs of RPV Clad Materials. (a) K001, (b) K002, white = Austenite, black = δ ferrite

3. Results and Discussion

3.1. Microstructure of RPV Clads

There was no distinctive feature of microstructural differences in the RPV clads regardless of the maximum heat input rate during overlay cladding. The overall distribution and amount of ferrite phase was almost the same irrespective of test samples. Fig. 2 shows a distribution of δ ferrite along the austenite grain boundaries or sometimes inside the austenite matrix in a skeleton manner. However, as listed in Table 2, the higher heat input prior to PWHT (K002) gave slightly larger amount of ferrite phase than the lower one (K001). And, after the stress relieving heat treatment the ferrite content of each test sample was reduced to about 6 percent. This reduction of ferrite content could be explained by the decomposition of δ ferrite to new austenite, chromium rich carbide ($M_{23}C_6$ type) and σ phase during the PWHT [5, 6, 11]. In addition, in the case of K002 clad sample the total amount of σ phase was larger than that of K001 clad (Table 2). Fig. 3 shows the distribution of σ phase by eutectoid reactions in σ ferrite phase. The σ phase is a hard, intermetallic phase with a complex tetragonal structure and its occurrence has been associated with the degradation of mechanical properties [11, 12].

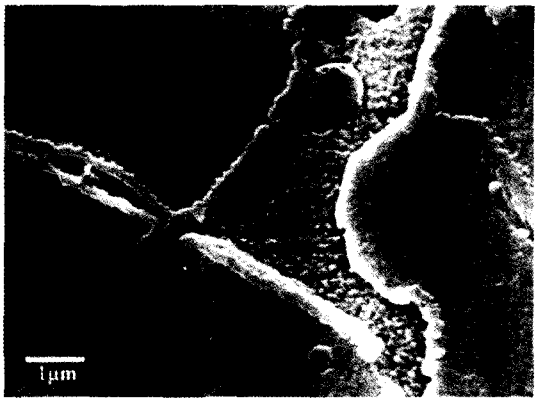

(a)

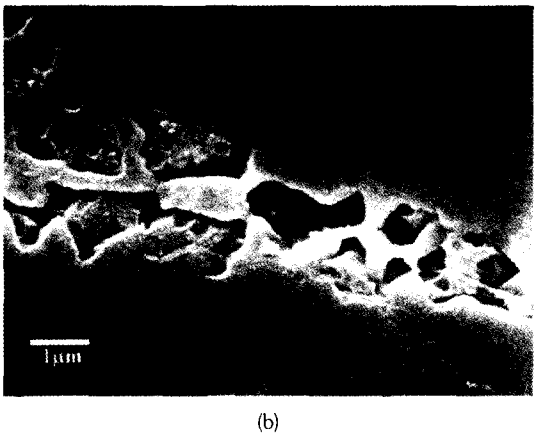

(b)

Fig. 3. Scanning Electron Micrographs Outlining Carbides Along the Grain Boundaries (a), Revealing Attacking Sigma Phase (b)

3.2. Mechanical Properties by SP Test

3.2.1. Temperature Dependent SP Load-deflection Curves

Fig. 4 presents the typical small punch load-deflection curves of K002 RPV clad at room temperature with the definition of mechanical properties by the SP test. It is reported that the deformation developed in the disk bending by the

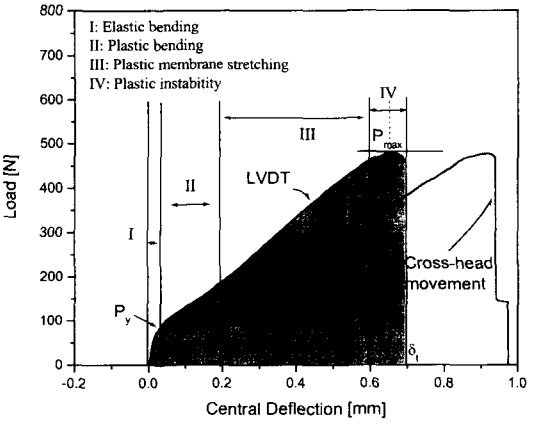

Fig. 4. Typical SP Load-deflection Curves of TEM Disk Type K002 Material with the Definition of SP Properties

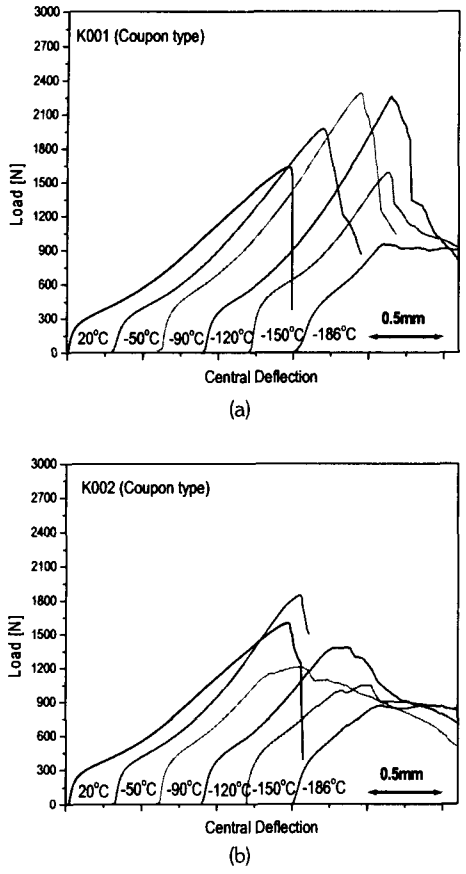

Fig. 5. Typical SP Load-deflection Curves of Coupon Type Specimens as a Function of Test Temperature. (a) K001, (b) K002 RPV Clad

SP test consists of four distinctive regimes: elastic bending, plastic bending, plastic membrane stretching, and plastic instability [7, 8, 13]. As the test temperature becomes low, the contribution of each deformation regime changes. Further, Fig. 4 reveals the large differences of deflections at the center of the SP specimen when the deflections were measured by cross head movement and LVDT. These discrepancies seem to be originated from the elastic deflection of loading pin and system compliance [13]. In the following section, therefore, only the results of LVDT measurement were used to evaluate the various SP properties.

Fig. 5 presents the typical load-deflection curves of coupon type SP specimens as a function of test temperature. Above -120℃, in the case of K001 clad, the abrupt load drop after the maximum load can be seen, which corresponds to the plastic instability regime. And below -120℃, a load drop initially occurs and then the repeated rises and drops of load at plastic membrane stretching regime are observed until the final fracture of the SP specimen. These trends are thought to be related with the selective fracture of circumferential ferrite by the high radial stress (load drop) and the arrest by surrounding ductile austenite (load rise) at lower temperatures observed in the duplex stainless steel [10]. Similar behavior existed in the set of load-deflection curves regardless of SP specimen types and materials except for the onset temperature of the serrations.

3.2.2. Correlation Between Tensile and SP Properties

The empirical correlations between SP test and tensile test results have been established to find out the yield strength, tensile strength, and ductility from SP tests [7-9]. The yield load, P_y, intersection point of linearity between elastic and plastic bending regimes, and the maximum load, P_m, can be correlated to yield strength and ultimate tensile strength, respectively. In the present study, $t_0/20$ and $t_0/15$ offset lines from the tangent of elastic bending regimes are effective to determine the P_y of TEM disk and coupon type SP test results, respectively, where t_0 is the initial specimen thickness in millimeter (Fig. 6). The P_y and P_m loads are illustrated in Fig. 7 as a function of test temperature. When the P_y load is normalized by t_0^2, it resulted in almost similar stress level

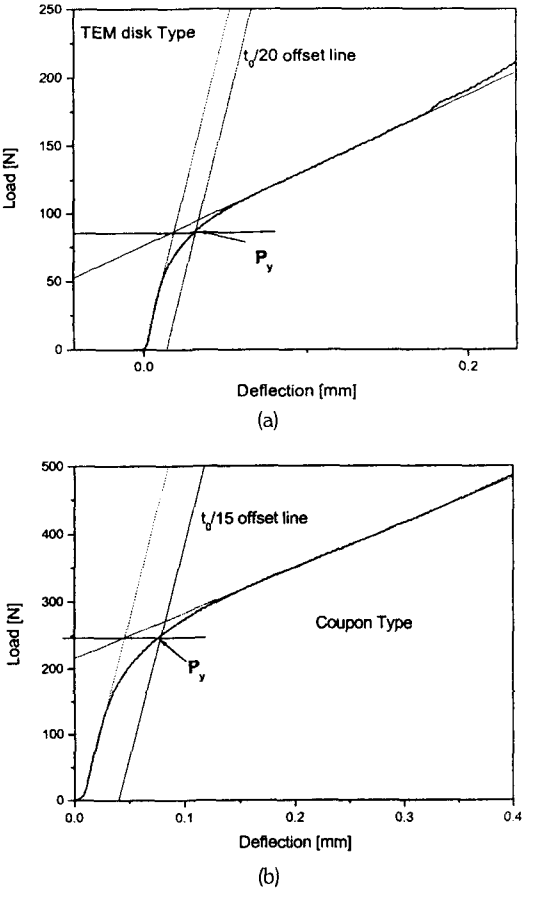

Fig. 6. Determination of SP Yield Load, P_y, Depending on the Specimen Types. (a) TEM Disk, (b) Coupon Type SP Specimen

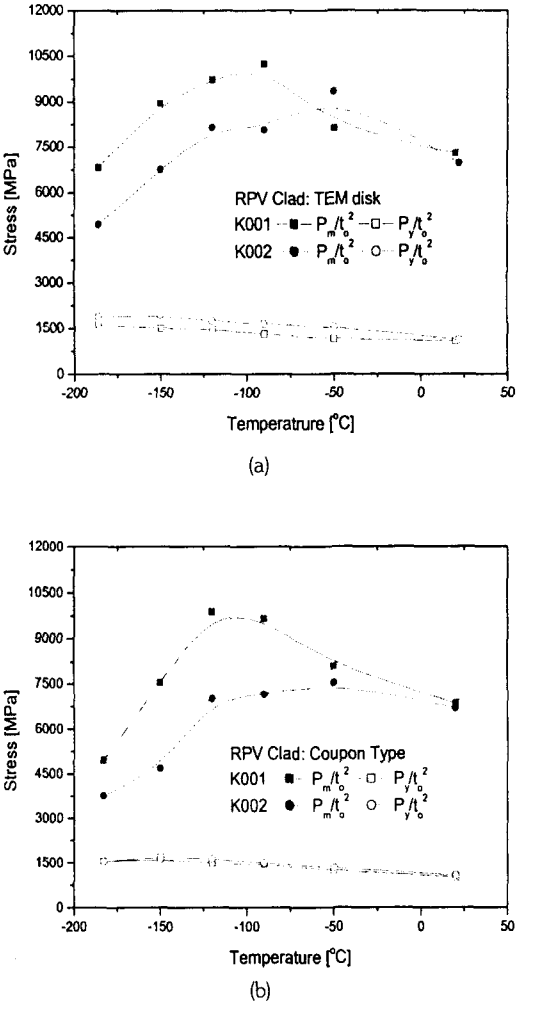

Fig. 7. Normalized Yield, P_y/t_o^2, and Maximum SP Load , P_m/t_o^2, as a Function of Test Temperature for K001 and K002 RPV Clads. (a) TEM Disk, (b) Coupon Type SP Specimen

regardless of SP specimen types and the K002 RPV clad exhibited a slightly higher P_y/t_0^2 value than the K001 material in all of the test conditions. But, the normalized maximum SP load showed a reversed trend such that the K002 material had lower P_m/t_0^2 values than those of K001 specimen. The maximum SP load, P_m, consists of four components corresponding to each deformation regime.

$$P_m = \Delta P_{eb} + \Delta P_{pb} + \Delta P_{pms} + \Delta P_{pi},$$

where, ΔP_{eb}, ΔP_{pb}, ΔP_{pms} and ΔP_{pi} represent the constituent of maximum SP load such a elastic bending, plastic bending, plastic membrane stretching and plastic instability, respectively. The components of elastic and plastic bending of the normalized maximum load were independent of test materials and gradually increased with

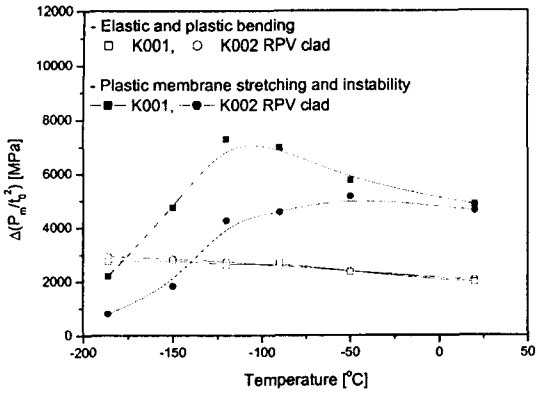

(a)

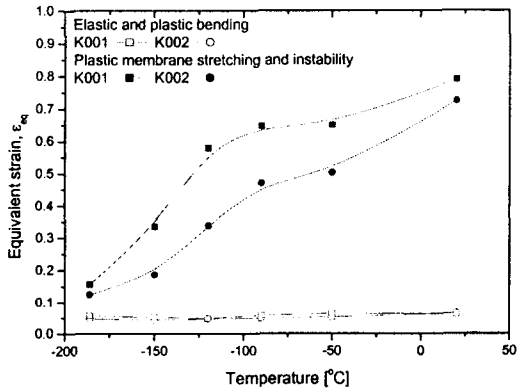

(b)

Fig. 8. The Components of Normalized Maximum SP Loads (a), and Equivalent Fracture Strain (b) as a Function of Temperature. The Equivalent Strain was Calculated by the Empirical Linear Relationship as Expressed in Section 3.2.3

decreasing temperature. But, the plastic membrane and instability components showed larger differences depending on test temperatures (Fig. 8(a)). These are related with the fact that the plastic strain of K002 clad, corresponding to the plastic membrane stretching and plastic instability, is smaller than that of K001 (Fig. 8(b)). Therefore, the reduction of plastic membrane stretching and plastic instability make the strengthening effects

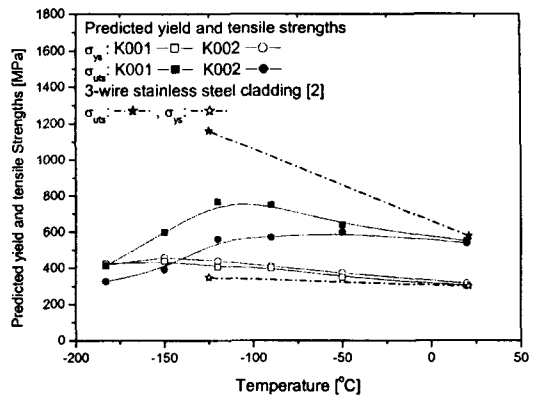

Fig. 9. The Predicted Yield and Tensile Strengths Based on the Linear Relationships of Normalized SP Load

much smaller at lower test temperatures.

Mao et al. [7] have derived an empirical linear relationship between normalized SP load and tensile properties. In the present work, the empirical linear relationships between the loads P_y, P_m and the yield and tensile strength were expressed by,

$$\sigma_y = 0.231(p_y/t_0^2) + 68.1$$
$$\sigma_{uts} = 0.071(P_m/t_0^2) + 60.03$$

where, σ_y and σ_{uts} are yield strength and ultimate tensile strength, respectively, and P_y/t_0^2 and P_m/t_0^2 are in MPa. The proportional constants were calculated from room temperature tensile and SP tests using various kinds of austenitic steels including both kinds of clad. Fig. 9 shows the predicted yield strength and tensile strength of RPV clad based on the above linear relationship. The predicted yield strengths are successful to evaluate the actual yield strengths of similar grade RPV clad, but, there may be no clear relationship between maximum load in SP test and ultimate tensile strength in tensile test, especially when the entire test temperature

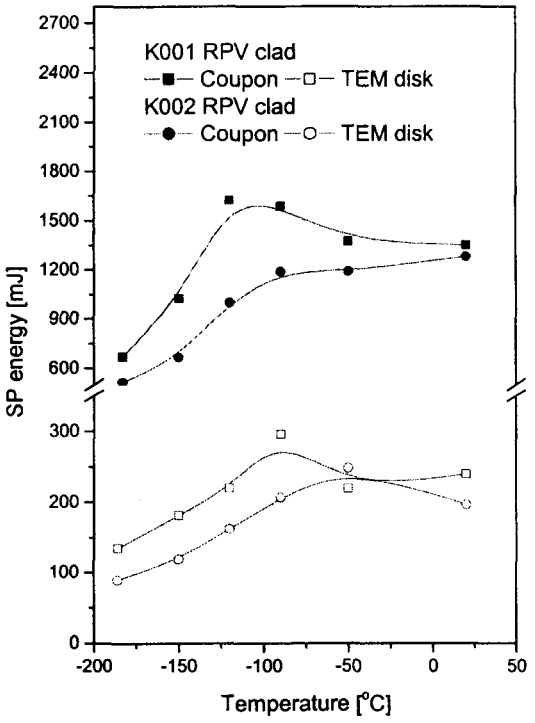

Fig. 10. The Temperature Dependent SP Energy Behavior of RPV Clad Specimens

region was considered.

3.2.3. Microstructure Dependent SP-DBTT Behavior

Fig. 10 presents the temperature dependent SP energy behavior of RPV clad materials in both types of SP specimens. SP energy is determined by the area under load-deflection curve. The coupon type K001 clad showed a gradual increase of SP energy with decreasing temperature until a maximum energy reached at around -120℃. As the test temperature decreased further, the abrupt drop of SP energy was observed. Similar trend was found in K002 clad results except it did not show the maximum SP energy, and the onset

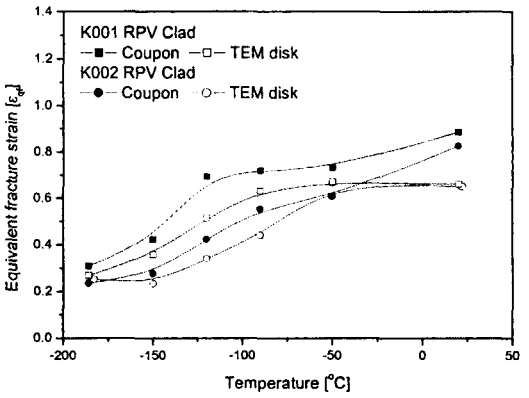

Fig. 11. The Equivalent Fracture Strain, ε_{qf}, Curves as a Function of Test Temperature

temperature of the abrupt drop of SP energy moved to higher temperature. The main reasons for these facts seem to originate from the intensity of grain boundary embrittlement depending on the amount of σ phase in ferrite phase (Table 2). Because the cracked σ phase at an early stage in the deformation process acted as voids, the presence of σ phase resulted in a significant reduction in ductility [11].

Comparing coupon and TEM disk type SP results, the temperature of maximum SP energy of TEM disk type was shifted about 20 ℃ to higher temperature in K001 clad. This discrepancy might result from the difference of stress and strain, which developed in the specimens with different specimen size.

Fig. 11 presents equivalent fracture strain curves as a function of test temperature. The equivalent fracture strain was evaluated by using the following empirical relationship [7, 9].

$$\varepsilon_{qf} = \ln(t_0/t^*) = \beta(\delta^*/t_0)^2$$

where, t^* and t_0 are the specimen thickness at the thinnest section and at the initial stage, respectively.

Table 4. SP-DBTT Data Depending on the Types of SP Specimen, Test Materials, and Determination Methods

	SP-DBTT (SP energy) [℃]		SP-DBTT (Equivalent fracture strain) [℃]	
	TEM disk	Coupon	TEM disk	Coupon
K001	-128.4	-146.9	-129.3	-140.6
K002	-107.5	-131.0	-90.0	-112.1
SP - ΔDBTT	20.9	15.9	39.3	28.5

β and δ^* are the proportional constant (0.09) and central deflection at fracture. As can be seen in Fig. 11, it reveals temperature dependent fracture strain behavior like those of SP energy except for the non-existence of peak fracture strain.

SP ductile-brittle transition temperature (SP-DBTT) is defined as the temperature where the SP energy is the average of maximum SP energy and lower shelf energy. But, these clad materials did not show the lower shelf energy up to the near liquid nitrogen temperature, it was calculated by using -186℃ SP data. Table 4 summarized the SP-DBTT data depending on the test materials and determination methods. According to the Table 4, K001 clad material showed lower SP-DBTT than K002 and the difference of SP-DBTT (SP-ΔDBTT) is 16~21 ℃. If SP-DBTT was determined by equivalent fracture strain, the SP-ΔDBTT is approximately twice as large as by the SP-ΔDBTT by the SP energy. In Fig. 11, SP-DBTT is defined as the temperature where the equivalent fracture strain is the average of upper and lower shelf. Although the absolute values of SP-DBTT and SP-ΔDBTT are different when those are determined by SP energy and equivalent fracture strain, they reveal a good consistency of transition temperature behavior.

3.2.4. Observation of Fracture Appearance for SP Specimens

Fracture surface observation following SP test revealed the fracture mode of each sample (Fig. 12). As expected, there were no big differences in fracture appearance regardless of test specimens. The cracking appearance was completely circumferential at room temperature. At −120℃, they showed the mixed mode of radial and circumferential cracking, and complete radial cracking was observed near at liquid nitrogen temperature.

In ductile disk bending, the peak of strain, which was a ring of the specimen around the pole, moved toward the clamped edge with continued deformation, and as the peak radial strain was much higher than the circumferential [14], the circumferential cracking was formed near at the clamped edge at room temperature. Below transition region, however, the plastic deformation was insufficient to move the peak of strain toward clamped edge because the ferrite phase was easily fractured by the high radial stress and combined with each other by the tearing of surrounding austenite [10]. Therefore, the main cracks were initiated near at the center of disk type SP specimen and propagated to the radial direction.

Fig. 12 (b) and Fig. 13 show that the dominant cracking process below the lower transition region was intergranular and quasi-cleavage fracture mode. These fracture profiles are thought to result from the preferential failure of ferritic phase at lower temperature [15], since the ferritic phases were inherently temperature sensitive.

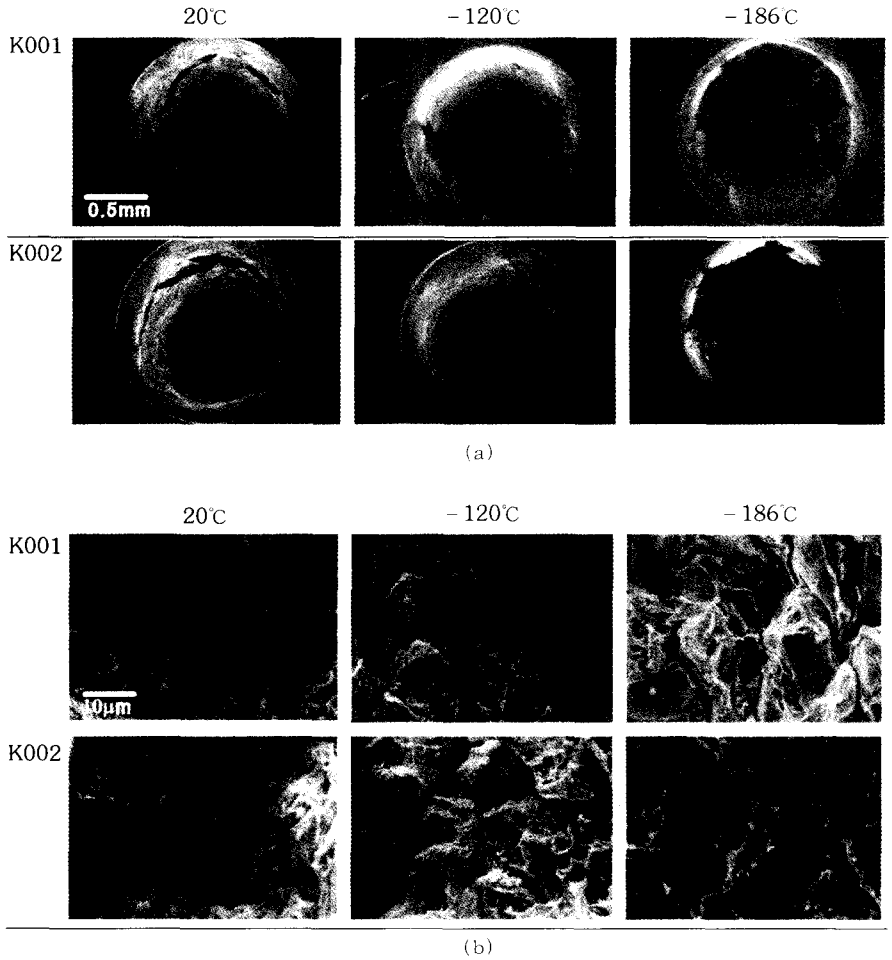

Fig. 12. SEM Images of TEM Disk Type RPV Clad SP Specimens. (a) Fracture Appearance, (b) Fracture Surface

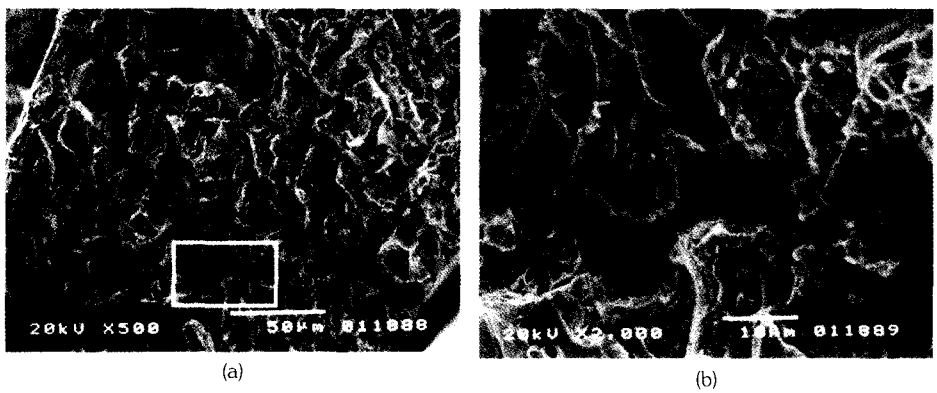

Fig. 13. SEM Images of TEM Disk Type K001 Specimen Tested at −186℃. (a) Through-thickness Fracture Surface, (b) Higher Magnification of the Region Indicated in (a)

4. Conclusions

From the small punch (SP) test on the RPV clad steel, the following conclusions can be drawn:

1. Although the RPV clad material had a small portion of ferrite phase, it still showed the ductile to brittle transition behavior like those of ferritic steels. Moreover, the SP transition temperature depended on the microstructure of RPV clad, specimen size, and determination methods. Equivalent fracture strain also provided consistent data for the evaluation of SP-DBTT with SP energy and the RPV clad embrittlement was influenced by the content of σ phase in ferrite phase, which gave rise to the increment of SP-DBTT.
2. As test temperature became low, the fracture appearance of SP specimen was changed from circumferential to radial cracking, and the dominant cracking process below the transition region was intergranular and quasi-cleavage fracture caused by low temperature failure of ferrite phase.

Acknowledgement

This work has been carried out as a part of the HANARO Utilizing Project under the Nuclear R&D Program by MOST, Korea. The authors are grateful to DooSan Heavy Industry for supplying of RPV clad materials as welded state.

References

1. M. G. Hortsten, W. P. A. Belcher, Fracture toughness and tensile properties of irradiated reactor pressure vessel cladding material, Effect of Radiation on Materials: 20th International Symposium, ASTM STP 1405, S.T. Rosinski et. al. Eds., ASTM, West Conshohocken, PA. (2001).
2. F. M. Haggag, Degradation of mechanical properties of stainless steel cladding due to neutron irradiation and thermal aging, Effect of Radiation on Materials: 16th International Symposium, ASTM STP 1175, A. S. Kumar et. al. Eds. ASTM, Philadelphia, (1993).
3. F. M. Haggag, W. R. Corwin, R. K. Nanstard, Effects of irradiation on the fracture properties of stainless steel weld overlay cladding, Nuclear Engineering and Design, 124, 129-141, (1990).
4. J. K. Sharples, D. P. G. Lidbury, M. G. Horsten, R. Pelli, State-of-the-art review of cladding materials data, Severe accidents and Other Topics in the RPV Design-2000, PVP-Vol. 403, ASME, 195-204, (2000).
5. J. A. Brooks, A. W. Thompson, Microstructural development and solidification cracking susceptibility of austenitic stainless steel welds, International Materials Reviews, Vol. 36, No. 1, 16-44, (1991).
6. K. M. Lee, H. S. Cho, D. C. Choi, Effect of isothermal treatment of SAF 2205 duplex stainless steel on migration of δ/γ interface boundary and growth of austenite, Journal of Alloys and Compounds, 285, 156-161, (1999).
7. X. Mao, H. Takahashi, Development of a further-miniaturized specimen of 3mm diameter for TEM disk small punch tests, Journal of Nuclear Materials, 150, 42-52, (1987).
8. X. Mao, T. Shoji, H. Takahashi, Characterization of fracture behavior in small punch test by combined recrystallization-etch method and rigid plastic analysis, Journal of Testing and Evaluation, Vol. 15, No. 1, 30-37, (1987).
9. T. Misawa, S. Nagata, N. Aoki, J. Ishizaka, Y. Hamaguchi, Fracture toughness evaluation of fusion reactor structural steels ay low

temperatures by small punch tests, Journal of Nuclear Materials, 169, 225-232, (1989).

10. J. S. Cheon and I. S. Kim, Evaluation of thermal aging embrittlement in CF8 duplex stainless steel by small punch test, Journal of Nuclear Materials, 278, 96-103, (2000).
11. C. C. Tseng, Y. Shen, S. W. Thompson, M. C. Mataya, G. Krauss, Fracture and the formation of sigma phase , $M_{23}C_6$, and austenite from delta-ferrite in an AISI 304L stainless steel, Metallurgical and Materials Transactions A, 25A, 1147-1158, (1994).
12. A. V. Kington and F.W. Noble, σ phase embrittlement of a type 310 stainless steel, Materials Science and Engineering, A138, 259-266, (1991).
13. T. S. Byun, E. H. Lee, J. D. Hunn, K. Farrell, L. K. Mansur, Characterization of plastic deformation in a disk bend test, Journal of Nuclear Materials, 294, 256-266, (2001).
14. A. K. Chosh, S. S. Hecker, Failure in thin sheets stretched over rigid punches, Metallurgical Transactions A, 6A, 1065-1074, (1975).
15. W. R. Cowin, R. G. Berggren, R. K. Nanstad, R. J. Gray, Fracture behavior of a neutron-irradiated stainless steel submerged arc weld cladding overlay, Nuclear Engineering and Design, 89, 199-221, (1985).